Microfluidic Digital Twin for Enhanced Single-cell Analysis

Samreen T. Mahmud[1 [0009−0004−6136−7364]], Wentao Ma[1 [0000−0002−6472−3385]], Taylor Thomsen[2,3 [0000−0002−5277−4935]], Chang Chen[2 [0009−0006−2790−3025]], Rachel Rex[2 [0009−0004−1017−3332]], Andre Lai[2,3 [0000−0003−3233−3590]], Lydia L. Sohn[2,3 [0000−0003−2195−2521]], and Amanda Randles[1 [0000−0001−6318−3885]]

[1] Dept of Biomedical Engineering, Duke University, Durham NC 27705, USA
{samreen.mahmud, wentao.ma, amanda.randles}@duke.edu
[2] Dept of Mechanical Engineering, University of California at Berkeley, Berkeley CA 94720-1740, USA
[3] UC Berkeley–UC San Francisco Graduate Program in Bioengineering, University of California, Berkeley CA 94720 USA {taylorthomsen, chang.chen, rachelrex, andre.lai, sohn}@berkeley.edu

Abstract. Advancing single-cell analysis requires tools that not only enable precise experimental measurements but also offer predictive capabilities to guide device optimization and expand experimental possibilities. This study addresses this need by developing a digital twin framework for mechano-node-pore sensing (mechano-NPS), a high-throughput microfluidic platform for single-cell analysis. By creating a virtual replica that integrates models of fluid dynamics and cellular behavior, the digital twin serves as a critical tool for both device development and hypothesis exploration. The foundation of the digital twin was established by accurately modeling the fluid dynamics within the mechano-NPS device, with simulations at various inlet pressures verified against analytical solutions. To ensure biological relevance, cellular models were rigorously tested to replicate key behaviors within the platform. The digital twin's performance was validated against experimental data, focusing on cell velocity and whole cell deformation index (wCDI). While variances in cell velocity highlighted systematic biases, the strong agreement of simulated wCDI with experimental results underscores the digital twin's reliability. This framework not only demonstrates the potential to enhance the mechano-NPS platform but also exemplifies how digital twins can transform experimental approaches in cellular biology.

Keywords: Digital twin · Microfluidic device · Single-cell analysis

1 Introduction

Microfluidic platforms have revolutionized cellular biology by enabling precise single-cell analysis and integrating multiple processes within a single device, paving the way for micro total analysis systems (μTAS) [1, 2]. However, the

ICCS Camera Ready Version 2025
To cite this paper please use the final published version:
DOI: 10.1007/978-3-031-97626-1_20

traditional strategy to developing these platforms is often highly involved, time-intensive, and experimentally limiting, restricting their optimization and overall impact [2, 3]. A digital twin framework for microfluidic devices addresses this critical gap by creating a virtual replica that not only accelerates design and optimization but also provides detailed insights into physical phenomena that are difficult or impossible to measure in conventional experimental setups. Computational modeling enables the exploration of key parameters such as velocity and pressure fields, shear stresses and forces on the cell surface, and mass and heat transfer [2]. For single-cell analysis, where microfluidic platforms currently offer high throughput but limited measurable parameters, digital twins dramatically expand the scope of accessible data. This integration enhances our understanding of device functionality and the underlying pathophysiology, transforming experimental microfluidic platforms into more versatile and informative tools for cellular biology.

Optimizing device geometry and operating parameters is crucial for improving microfluidic platform performance. Digital twins facilitate rapid assessment of numerous variables while ensuring efficient functionality. Computational studies have been utilized to identify optimal pillar spacings to improve device performance [4], investigate the impact of pillar cross-sections and alignments on fluid distribution in the device [5], and analyze the effect of inlet conditions for the separation of circulating tumor cells (CTC) in a microfluidic chip [6]. In addition to optimizing the operation parameters of a microfluidic device, computational models are invaluable for investigating fluid flow properties that influence the functionality of a microfluidic device, such as velocity distribution and fluid-induced shear stress. These models have been used to replicate different shear flow conditions in microfluidic devices [7] and to study the effects of shear stress in cell cultures [8, 9].

Beyond fluid flow, computational models have played a significant role in investigating cellular mechanics within microfluidic environments. For instance, Esposito et al. employed three-dimensional (3D) numerical simulations to examine the influence of fluid inertia on cell softness in cylindrical and rectangular microchannels, aiding in cell sorting based on mechanical characteristics [10]. Tan et al. used immersed boundary methods to examine how cells squeeze through micropores of varying sizes under different pressures, establishing cell deformability as a potential biomarker [11]. Similarly, Hynes et al. modeled CTCs as rigid and deformable spheres within a bioprinted vascular chip to assess mechanical interactions [12]. Despite these advances, experimental limitations persist in measuring critical cellular parameters such as stiffness and forces exerted on the cells. Computational tools provide a crucial bridge, supplementing experiments with in silico models to extract insights that would otherwise be inaccessible. For example, Deng et al. integrated computational modeling with an inertial microfluidic cell stretcher (iMCS) to measure the isoshear modulus of cell membranes, an elusive parameter in purely experimental setups [13]. Similarly, Sadaat et al. combined microfluidic experiments with simulations to determine the shear modulus of red blood cells (RBCs) [14]. However, these approaches

ICCS Camera Ready Version 2025
To cite this paper please use the final published version:
DOI: 10.1007/978-3-031-97626-1_20

often require high-speed imaging systems, making them costly and less accessible. The integration of digital twins with microfluidic devices presents a scalable and cost-effective alternative, enhancing experimental capabilities while reducing expensive hardware.

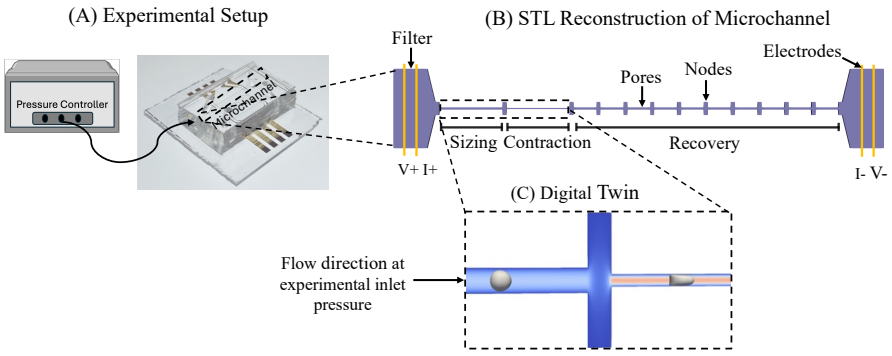

Fig. 1. ((A) Fabricated microfluidic device for driving cells through a channel under constant pressure. (B) Reconstructed geometry of the mechano-NPS platform with segmented channels, DC voltage applied via outer electrodes, and current measured by inner electrodes. (C) Digital twin simulating deformable cells and fluid flow using the STL geometry and experimental pressure inputs.

This work establishes a digital twin framework for the microfluidic device mechano-node-pore sensing (mechano-NPS), enhancing its single-cell analysis capabilities while maintaining high fidelity. Mechano-NPS is a mechanophenotyping platform based on the Coulter-counter technique of particle counting (Figure 1(A)) [15]. Unlike traditional high-speed optical techniques, mechano-NPS achieves a remarkable throughput of 300-500 cells per minute without relying on high-speed optical instruments or costly cameras [16]. Mechano-NPS operates by measuring the modulated electrical currents across a microfluidic channel segmented into nodes and pores (Figure 1(B)). The device includes a narrow contraction region, forcing cells to squeeze through, allowing measurement of key properties such as cell diameter, resistance to compressive deformation, transverse deformation, and recovery time after deformation. A novel whole cell deformability index (wCDI) quantifies cell stiffness, enabling differentiation of cell lineage, chronological age, and stage of malignant progression in human epithelial cells [16, 17]. Given its high throughput, cost-effectiveness, and multiparametric capabilities, mechano-NPS is ideally suited for integration with a digital twin to enhance its performance and expand its analytical capabilities.

To build the digital twin, we first verified the fluid flow within the device by comparing simulation results with analytical solutions, ensuring accuracy in modeling a fundamental aspect that directly influences cell behavior. This robust fluid flow model served as the foundation for further development. Next,

ICCS Camera Ready Version 2025
To cite this paper please use the final published version:
DOI: 10.1007/978-3-031-97626-1_20

we verified the computational representation of cellular behavior by comparing simulated cell velocities against analytical solutions, demonstrating the model's ability to replicate experimental conditions and predict outcomes reliably. Finally, we validated the digital twin against experimental data comparing cell velocity in different device segments and wCDI under various inlet conditions.

Through this work, we present a comprehensive digital twin framework for mechano-NPS that extends its experimental reach and analytical power. By enabling measurement of additional parameters, rapid exploration of design modifications, and optimization of the device performance, this digital twin transforms mechano-NPS into an even more powerful tool for single-cell analysis. More broadly, this approach highlights the potential of digital twins in microfluidic research, paving the way for scalable, data-driven advancements in cellular biomechanics.

2 Methods

2.1 Experimental Setup

The mechano-NPS platform is fabricated using soft lithographic techniques, as previously published [16, 17]. Briefly, polydimethylsiloxane (PDMS) mold of the mechano-NPS channel is cast from a silicon negative-relief master mold, the height of which is approximately 20 μm. Once excised, the PDMS mold is bonded to a glass substrate with pre-defined platinum electrodes and gold contact pads that were fabricated using traditional lithography and electron-gun evaporation (Figure 1(A)). As shown in the schematic of Figure 1(B), the mechano-NPS channel is comprised of three regions: sizing, contraction, and recovery. The sizing and the contraction segments are 800 μm in length, and the recovery node-pores are each 285 μm in length. The nodes segment the overall channel to provide spatio-temporal resolution and are 85 μm wide, and 50 μm long. Filters are included at the inlet reservoir to exclude cell aggregates and cellular debris. The dimensions of the channel were chosen to provide sufficient transit time while maintaining a high signal-to-noise ratio (SNR).

Human promyelocytic (HL60) cells were introduced into the microfluidic channel under two separate non-pulsatile pressures of 11 and 15 kPa. The modulated current pulse produced by a cell transiting the mechano-NPS was measured using a four-point probe. Current with respect to time was recorded, low-pass filtered, and then processed with a custom-written code [18] to extract information such as magnitude and duration for each pulse event for further analysis.

2.2 Computational Model

To develop a digital twin of mechano-NPS, we utilized the massively parallel computational fluid dynamics solver HARVEY [19, 20] to simulate fluid dynamics within a microfluidic device. Cells were explicitly modeled in the microfluidic channel as shown in 1(C) to represent the HL60 cell line, incorporating five

ICCS Camera Ready Version 2025
To cite this paper please use the final published version:
DOI: 10.1007/978-3-031-97626-1_20

different cell sizes to account for cellular heterogeneity. HARVEY implements the lattice Boltzmann method (LBM) to solve the governing fluid equations, whereas cells are modeled using the finite element method (FEM) and are coupled to surrounding fluid using the immersed boundary method (IBM).

LBM for Fluid Flow LBM is a deterministic, mesoscopic approach that numerically solves the Navier-Stokes equations by modeling fluid with a particle distribution function. Fluid behavior is discretized using a fixed Cartesian lattice, where the probability function $f_i(\mathbf{x}, t)$ determines the probability of finding a particle at lattice point $\mathbf{x}$ and time t with a discrete velocity $\mathbf{c}_i$ [21]. The evolution of the particles with an external force field is governed by [22]:

$$f_i(\mathbf{x} + \mathbf{c}_i, t + 1) = \left(1 - \frac{1}{\tau}\right) f_i(\mathbf{x}, t) + \frac{1}{\tau} f_i^{eq}(\mathbf{x}, t) + F_i(\mathbf{x}, t) \tag{1}$$

where $f_i^{eq}(\mathbf{x}, t)$ is the Maxwell-Boltzmann equilibrium distribution and F_i is the external force field. HARVEY employs a D3Q19 velocity discretization model with the Bhatnagar–Gross–Krook (BGK) collision operator $\Omega = 1/\tau$, where τ is the relaxation time which determines the relaxation of f_i towards the equilibrium distribution function f_i^{eq}. The kinematic viscosity, ν is linked to τ by $\nu = c_s^2(\tau - 1/2)$ with a lattice speed of sound $c_s = 1/\sqrt{3}$. The density ρ and the velocity $\mathbf{v}$ are calculated respectively as the 0^{th} and the 1^{st} moment of the distribution function, which are then used to calculate the equilibrium distribution function $f_i^{eq}(\mathbf{x}, t)$. The external force $F_i(\mathbf{x}, t)$ that accounts for the body force imparted by the cell on the fluid is calculated by applying Guo's forcing scheme [23]. At the walls, no-slip condition is enforced using the halfway bounce-back boundary conditions whereas a constant density at the inlets and outlets is applied using a Zou-He like algorithm adapted to the D3Q19 velocity discretization [24]. The fluid is simulated with a density of 1000 kgm^{-3} and a viscosity of 0.89 mPa.s at a lattice grid spacing of 0.125 μm.

FEM for Deformable Cells Deformable cells are modeled as fluid-filled capsules with a triangulated membrane of zero thickness having an initial spherical shape [25, 20] using FEM. For simplicity, the cytoplasm is considered an incompressible Newtonian fluid having the same kinematic viscosity as the ambient fluid representing the cytoskeleton while neglecting the nucleus. The cell membrane is modeled to be isotropic and hyperelastic which follows the Skalak constitutive law for resisting shear and area dilation [26]. The strain energy function is given by:

$$W_s = \frac{G_s}{4}[(I_1^2 + 2I_1 - 2I_2) + CI_2^2] \tag{2}$$

where G_s is the shear elastic modulus, I_1 and I_2 are the strain invariants of the Green strain tensor, and C is the ratio of dilation to shear modulus. The membrane's resistance to bending is implemented using the Helfrich formulation [27]. The HL60 cells were modeled with a shear elastic modulus, G_s, of 2.25 $\times$

ICCS Camera Ready Version 2025
To cite this paper please use the final published version:
DOI: 10.1007/978-3-031-97626-1_20

10^{-4} Nm^{-1} and a bending modulus, E_b, of 1×10^{-18} J to match the behavior of the cell observed experimentally.

IBM for Coupling To account for the interaction of the cell with the ambient fluid, the Lagrangian grid of the FEM cell model is coupled to the Eulerian grid of LBM by applying IBM [28]. Here, three components of IBM are implemented with the following sequence: interpolation, updating, and spreading. At first, to determine the cell membrane deformation, Lagrangian membrane velocity $\mathbf{V}$ is interpolated from the Eulerian velocity $\mathbf{v}$ with a three-dimensional Dirac delta function δ having four-point support as follows:

$$\mathbf{V}(\mathbf{X}, t) = \sum_{\mathbf{x}} \mathbf{v}\delta(\mathbf{x} - \mathbf{X}(t)) \tag{3}$$

where $\mathbf{X}$ is the vertex location of the Lagrangian grid and $\mathbf{x}$ is the fluid lattice location in the Eulerian grid. Next, we update the position of the cell vertex with a no-slip condition, assuming unit timesteps. Lastly, the forces calculated at each Lagrangian vertex $\mathbf{G}$ are spread onto the surrounding Eulerian grid using the same delta function:

$$\mathbf{g}(\mathbf{x}, t) = \sum_{\mathbf{X}} \mathbf{G}(\mathbf{X}, t)\delta(\mathbf{x} - \mathbf{X}(t)) \tag{4}$$

3 Results and Discussions

3.1 Verification of fluid flow in microfluidic digital twin against analytical solution

Accurate fluid flow modeling within mechano-NPS is essential for ensuring the validity of the digital twin, as fluid dynamics directly influence cell velocity and deformation. As an initial verification step, we simulated fluid-only flow within the microfluidic device using our LBM-based model, excluding device filters from the simulation. As these filters do not induce a pressure drop and only serve to prevent cell aggregates or debris from clogging the entrance of the sizing pore, their omission does not affect the core flow dynamics. The fluid flow was analyzed at two different inlet pressures: 11 and 15 kPa. Upon convergence of the flow, we assessed the magnitudes of pressure and velocity along the centerline of the device, as shown in Figures 2(A) and ref fig:fluidprofile(B). The pressure profiles demonstrated a steady decline from the inlet pressure to zero at the outlet, with a consistent slope throughout each section. As expected, the most significant pressure drop occurred within the contraction pore, where the channel narrows, while the wider node sections exhibited minimal pressure variations. This behavior is characteristic of Poiseuille flow, confirming the expected pressure distribution.

The velocity profile demonstrated a consistent magnitude within each section of the device, aligning qualitatively with Poiseuille flow characteristics. At both

ICCS Camera Ready Version 2025
To cite this paper please use the final published version:
DOI: 10.1007/978-3-031-97626-1_20

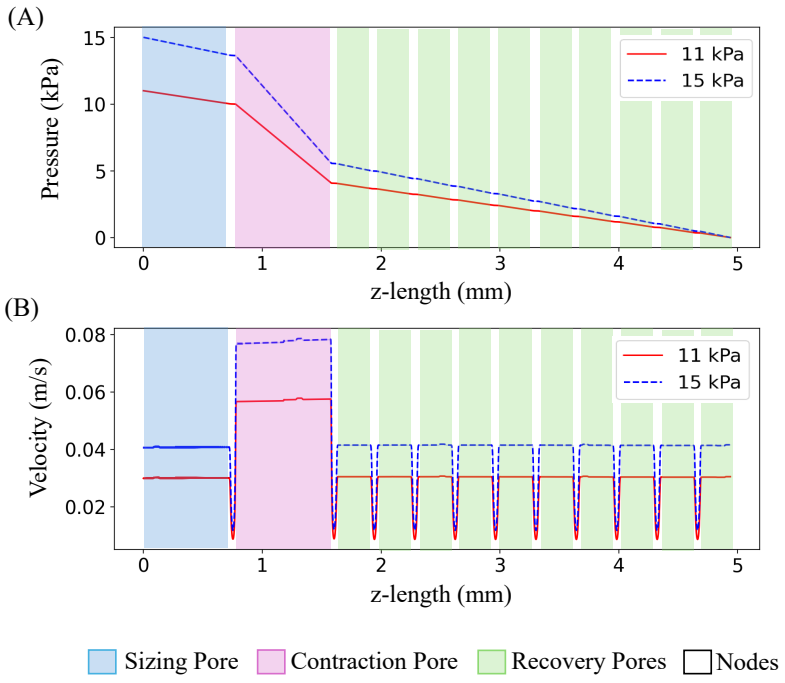

Fig. 2. (A) Pressure and (B) Velocity profiles across the mechano-NPS platform modeled with the digital twin at inlet pressures of 11 kPa and 15 kPa.

11 kPa and 15 kPa inlet pressures, the sizing and recovery pores exhibited similar velocities due to their identical dimensions. In contrast, the contraction pore, being the narrowest section, exhibited the highest velocities, while the nodes showed minimal velocity, as illustrated in Figure 2(B). To quantitatively verify the simulated fluid velocity, we compared our results to the analytical velocity profile of Poiseuille flow. Our analysis concentrated on two critical segments: the sizing pore, where cells move freely, and the contraction pore, where significant cell deformations occur. Given that the recovery pores mirror the sizing pore in design, they exhibit identical velocity characteristics, making the sizing pore analysis representative of both regions. The longitudinal velocity profile for a rectangular channel is given by [29]:

$$u_x(y,z) = \frac{16a^2}{\mu\pi^3}\left(-\frac{dp}{dx}\right)\sum_{i=1,3,5,\ldots}^{\infty}(-1)^{(i-1)/2}\left[1-\frac{\cosh(i\pi z/2a)}{\cosh(i\pi b/2a)}\right]\frac{\cos(i\pi y/2a)}{i^3}. \tag{5}$$

In Equation (5), a and b are the two widths of the rectangular cross-section, with $-a \leq y \leq a$ and $-b \leq z \leq b$, so the centerline velocity can be found by setting $y = z = 0$. x is the flow direction, so $-dp/dx$ is the pressure gradi-

ICCS Camera Ready Version 2025
To cite this paper please use the final published version:
DOI: 10.1007/978-3-031-97626-1_20

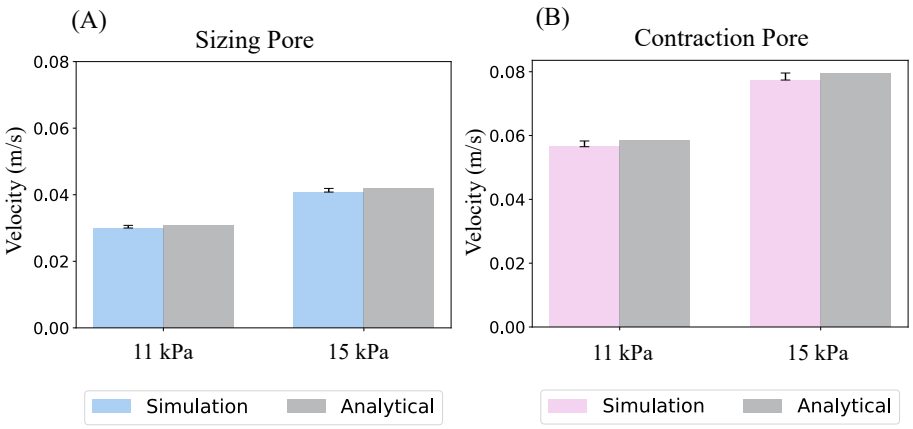

Fig. 3. Comparison of simulated velocities in (A) sizing and (B) contraction pores with analytical results.

ent driving the flow. The above equation gives a relation between the pressure gradient and the longitudinal velocity. Therefore, after obtaining the pressure gradient from Figure 2(A), we could calculate the analytical centerline velocity using Equation (5) for both the sizing and the contraction pores. The simulated velocity profiles closely matched the analytical solutions, with a percentage error of less than 4% at both 11 kPa and 15 kPa (Figure 3). This strong agreement confirms the accuracy of our fluid flow model, establishing a robust foundation for subsequent simulations involving cellular transport and deformation.

3.2 Verification of simulated cell velocity in a square channel and the sizing pore

To verify the accuracy of the cell velocity modeling, we performed simulations of cells moving through a fluid-filled square channel and compared the results with analytical solutions from [30], which were previously validated against experimental data. For this study, we constructed a square channel with a side length of 20 μm and a longitudinal length of 350 μm, replicating the dimensions used in the experimental validation.Three cell diameters: 10, 14, and 17 μm were studied in the square channel. Given the fluid and cell parameters, the Reynolds number and the size ratio between the cells and the channel closely resemble those within the sizing pore of the microfluidic device. Therefore, simulations conducted in the square channel serve as appropriate validation tests for assessing the digital twin's ability to accurately capture the physics within the sizing pore.

Figure 4 compares the simulated and analytical results for cell mobility. The horizontal axis represents the cell-to-channel size ratio, while the vertical axis shows the ratio of cell velocity to undisturbed centerline fluid velocity for each cell size. The results demonstrate a strong agreement between the simulation and

ICCS Camera Ready Version 2025
To cite this paper please use the final published version:
DOI: 10.1007/978-3-031-97626-1_20

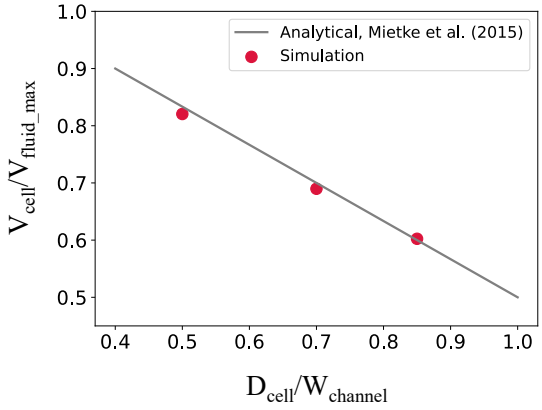

Fig. 4. Verification of cell model through comparison with analytical solutions in a square channel.

the analytical solutions. Although the analytical solution is based on rigid beads, it effectively captures the physics of cell mobility in both the simulated square channel and the sizing pore. This agreement is due to the small cell-to-channel size ratio (<0.9), where cell deformation (quantified by the non-dimensional capillary number) is negligible. In particular, Ahmmed et al. [31] measured the velocity of various cancer cells in a square microchannel and found that their results also aligned with analytical solutions for rigid beads. Similarly, Kuriakose et al. [32] reported that the capillary number—and thus cell deformation—had minimal influence on cell mobility in their experiments.

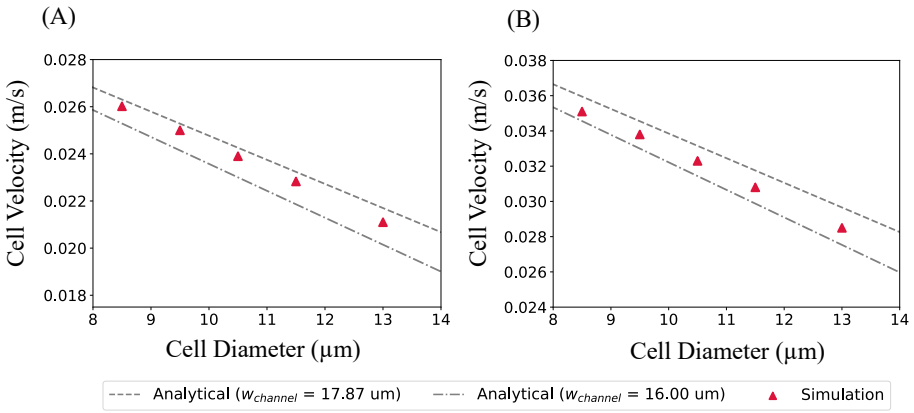

Fig. 5. Verification of cell model through comparison with analytical solutions in the sizing pore.

ICCS Camera Ready Version 2025
To cite this paper please use the final published version:
DOI: 10.1007/978-3-031-97626-1_20

Building on these analytical solutions for square channels, we infer the expected analytical cell velocity within the sizing pore, which has a rectangular cross-section. In Figure 5, the two lines in each subplot represent the analytical cell velocity for square channels with widths of 17.87 and 16.0 μm, corresponding to the two edges of the sizing pore cross-section. Since the dimensional difference between these edges is small, the actual analytical cell velocity is expected to fall between these two bounds, aligning well with the simulated data points. Thus, our simulations successfully validate cell velocity in the sizing pore, further reinforcing the accuracy of the digital twin model.

3.3 Validation of the simulated cell velocities and wCDI against experimental data

After successfully verifying our fluid and cell models, we proceeded to validate the digital twin using experimental data from HL60 cell screening with mechano-NPS. Given the substantial computational demands of simulating the cell transiting throughout the entire device, we focused our analysis on a key region of interest, depicted in Figure 1(C). This section consists of the sizing and contraction pores, where the cell first moves undeformed through the sizing pore before undergoing significant deformation in the contraction pore. To ensure consistency, input conditions were carefully tuned to match the flow characteristics throughout the device. To account for cellular heterogeneity, we selected five distinct cell sizes from the experimental data set, reflecting the natural size variation of HL60 cells. Validating the digital twin against experimental results is essential for ensuring its reliability and accuracy in predicting real-life scenarios. Our validation process focused on key performance metrics, that include cell velocities within the sizing and contraction pores which are critical components of the mechano-NPS platform. Additionally, we assessed the wCDI by comparing simulation-derived values with experimental measurements across a range of cell diameters, demonstrating the digital twin's capability to replicate experimental observations. The wCDI serves as an indicative measure of cell stiffness, which can be assessed using the mechano-NPS device and is defined as:

$$wCDI = (\frac{V_c}{V_0})(\frac{d_0}{h}) \tag{6}$$

where V_c is the cell velocity in the contraction pore, V_0 is the average cell velocity for all the different cell sizes in the sizing pore, d_0 is the cell's initial diameter, and h is the height of the channel. Cell velocities at an inlet pressure of 11 kPa were analyzed in both the sizing and contraction pores and compared with experimental data, as illustrated in Figures 6(A) and 6(B), respectively. The results revealed a consistent trend across both datasets: cell velocity decreased as cell diameter increased in both the sizing and contraction pores, as expected. However, a constant bias was observed between the simulation and experimental data, with identical slopes but differing intercepts due to this bias. To investigate the source of the discrepancy, we conducted an additional analysis at an input

ICCS Camera Ready Version 2025
To cite this paper please use the final published version:
DOI: 10.1007/978-3-031-97626-1_20

pressure of 15 kPa, as shown in Figure 7. The results reproduced the same bias, again showing identical slopes across datasets. Given the prior validation of the cell model and the consistency of this bias across inlet pressures, the discrepancy likely stems from a systematic difference between the experimental and simulation setups rather than an issue with the digital twin itself.

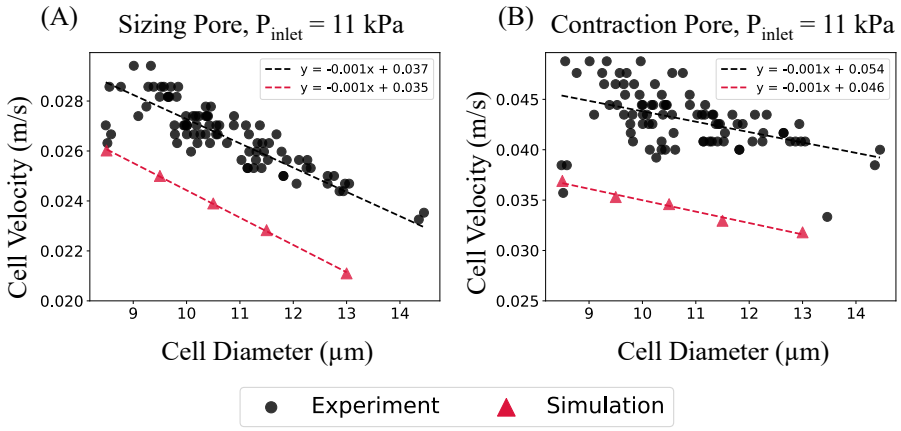

Fig. 6. Comparison of experimental and simulated cell velocities at 11 kPa inlet pressure in (A) sizing and (B) contraction pores.

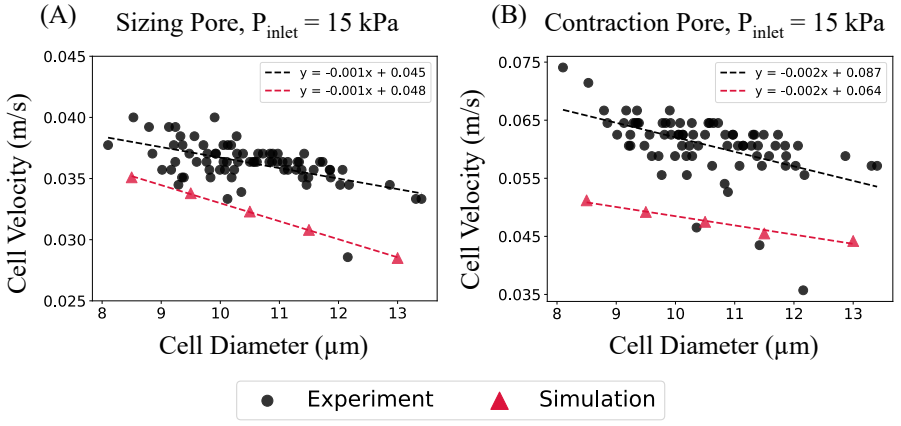

Fig. 7. Comparison of experimental and simulated cell velocities at 15 kPa inlet pressure in (A) sizing and (B) contraction pores.

ICCS Camera Ready Version 2025
To cite this paper please use the final published version:
DOI: 10.1007/978-3-031-97626-1_20

In validating the digital twin, a key objective was to accurately replicate the experimental wCDI, a novel parameter used by mechano-NPS to characterize cell stiffness. As wCDI is derived from the ratio of velocities in the sizing and contraction pores (Equation 6), its validation required first confirming the velocities in both regions. Despite the presence of a systematic bias in velocity measurements, this bias was effectively neutralized in the wCDI calculations due to the use of velocity ratios, leading to strong alignment between the experimental and simulated wCDI values. Figures 8(A) and 8(B) compare experimental and simulated wCDI at inlet pressures of 11 kPa and 15 kPa, respectively. At 11 kPa, the experimental and simulated wCDI values agreed closely, with a percent difference of less than 4% for all cell sizes except for the 8.5 μm cell, which showed a slightly higher 7% difference. This deviation can be attributed to the presence of outliers in cell velocity measurements at that size, as observed in Figure 6. For an inlet pressure of 15 kPa, the percent difference between the experimental and simulated wCDI values remained below 5%, further demonstrating strong agreement between the two data sets. To further assess these differences and evaluate the digital twin's capability in capturing cell behavior within the mechano-NPS device, a Bland-Altman analysis was conducted. The results revealed a bias close to zero, indicating no systematic difference between the two measurement approaches. The 95% limits of the agreement confirmed that the simulated wCDI values closely matched the experimental results. These findings underscore the reliability of the digital twin in accurately replicating cell behavior across varying test conditions within the mechano-NPS device, reinforcing its potential as a robust tool for in silico cell analysis and device optimization.

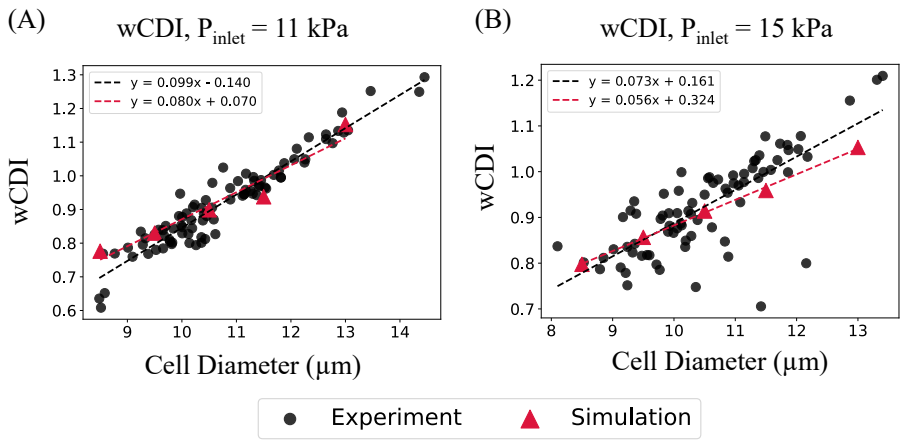

Fig. 8. Comparison of experimental and simulated wCDI at (A) 11 kPa and (B) 15 kPa inlet pressures.

ICCS Camera Ready Version 2025
To cite this paper please use the final published version:
DOI: 10.1007/978-3-031-97626-1_20

4 Conclusion

Microfluidic devices have become indispensable in single-cell analysis, enabling precise investigations into live-cell states, mechanical properties, and molecular components. Integrating these platforms with digital twins presents a transformative opportunity to accelerate cost-effective device optimization, providing access to otherwise unmeasurable parameters, and enhancing throughput without compromising accuracy. Beyond improving efficiency, digital twins also deepen our understanding of the fundamental physical principles governing microfluidic devices and the complex biological phenomena they interrogate.

In this work, we introduce a digital twin framework for mechano-NPS, a high-throughput microfluidic platform designed for single-cell mechanophenotyping. The framework replicates the experimental setup by integrating fluid dynamics and cellular behavior models to provide an accurate in silico representation of the system. Development began with rigorous fluid flow modeling, ensuring that simulated pressure and velocity distributions closely matched analytical solutions, thereby providing a robust foundation. Building on this, we developed and verified a cellular model that accurately represents the mechanical behavior of the cell within the device, ensuring the reliability of the digital twin for future predictions. Finally, the digital twin was validated against experimental data, focusing on key performance metrics such as cell velocity and wCDI. Although minor discrepancies in cell velocity were observed, the simulated wCDI closely matched the experimental results, underscoring the accuracy and robustness of the digital twin. While this study focuses on a specific platform, the proposed algorithm is generalizable and can be adapted to simulate a wide range of microfluidic devices in silico. A key challenge in implementing such digital twin models lies in the significant computational cost. Finite element method (FEM)-based modeling of cellular behavior demands high spatial resolution to capture accurate physical interactions, particularly when simulations are customized for specific experimental configurations. This requirement can lead to a trade-off between model fidelity and computational efficiency. Nevertheless, this limitation can be partially alleviated by leveraging scalable cloud computing resources, enabling broader accessibility and faster turnaround for high-fidelity simulations.

This work highlights the transformative potential of digital twins in experimental microfluidics, demonstrating their ability to extend capabilities, optimize performance, and unlock new avenues of discovery. By bridging computational modeling with experimental biology, digital twins redefine how microfluidic devices are designed, tested, and utilized, paving the way for the next generation of high-throughput, data-driven cellular analysis platforms.

5 Acknowledgments

The authors thank Jorik Stoop for fruitful discussions. This work was supported by NIH 5R01EB024989. The content does not necessarily represent the official views of the NIH. An award of computer time was provided by the INCITE

ICCS Camera Ready Version 2025
To cite this paper please use the final published version:
DOI: 10.1007/978-3-031-97626-1_20

program. This research used resources of the Argonne Leadership Computing Facility, which is a DOE Office of Science User Facility supported under Contract DE-AC02-06CH11357.

References

1. Yin, H., Marshall, D.: Microfluidics for single cell analysis. Current opinion in biotechnology **23**(1), 110–119 (2012)
2. Carvalho, V., Rodrigues, R.O., Lima, R.A., Teixeira, S.: Computational simulations in advanced microfluidic devices: A review. Micromachines **12**(10), 1149 (2021)
3. Sheidaei, Z., Akbarzadeh, P., Kashaninejad, N.: Advances in numerical approaches for microfluidic cell analysis platforms. Journal of Science: Advanced Materials and Devices **5**(3), 295–307 (2020)
4. Jun-Shan, L., Zhang, Y.-Y., Zhong, W., Jia-Yi, D., Xuan, Y., Ri-Ye, X., *et al.*: Design and validation of a microfluidic chip with micropillar arrays for three-dimensional cell culture. Chinese Journal of Analytical Chemistry **45**(8), 1109–1114 (2017)
5. Chen, W.-X., Li, J.-G., Wan, X.-H., Zou, X.-S., Qi, S.-Y., Zhang, Y.-Q., *et al.*: Design of a microfluidic chip consisting of micropillars and its use for the enrichment of nasopharyngeal cancer cells. Oncology letters **17**(2), 1581–1588 (2019)
6. Zhang, X., Xu, X., Ren, Y., Yan, Y., Wu, A.: Numerical simulation of circulating tumor cell separation in a dielectrophoresis based YY shaped microfluidic device. Separation and Purification Technology **255**, 117343 (2021)
7. Kou, S., Pan, L., van Noort, D., Meng, G., Wu, X., Sun, H., *et al.*: A multishear microfluidic device for quantitative analysis of calcium dynamics in osteoblasts. Biochemical and biophysical research communications **408**(2), 350–355 (2011)
8. Calibasi Kocal, G., Güven, S., Foygel, K., *et al.*: Dynamic microenvironment induces phenotypic plasticity of esophageal cancer cells under flow. Sci Rep. 2016,
9. Wong, J.F., Young, E.W., Simmons, C.A.: Computational analysis of integrated biosensing and shear flow in a microfluidic vascular model. AIP Advances **7**(11) (2017)
10. Esposito, G., Romano, S., Hulsen, M.A., D'Avino, G., Villone, M.M.: Numerical simulations of cell sorting through inertial microfluidics. Physics of Fluids **34**(7) (2022)
11. Tan, J., Sohrabi, S., He, R., Liu, Y.: Numerical simulation of cell squeezing through a micropore by the immersed boundary method. Proceedings of the Institution of Mechanical Engineers, Part C: Journal of Mechanical Engineering Science **232**(3), 502–514 (2018)
12. Hynes, W., Pepona, M., Robertson, C., Alvarado, J., Dubbin, K., Triplett, M., *et al.*: Examining metastatic behavior within 3D bioprinted vasculature for the validation of a 3D computational flow model. Science advances **6**(35), eabb3308 (2020)
13. Deng, Y., Davis, S.P., Yang, F., Paulsen, K.S., Kumar, M., Sinnott DeVaux, R., *et al.*: Inertial microfluidic cell stretcher (iMCS): fully automated, high-throughput, and near real-time cell mechanotyping. Small **13**(28), 1700705 (2017)
14. Saadat, A., Huyke, D.A., Oyarzun, D.I., Escobar, P.V., Øvreeide, I.H., Shaqfeh, E.S., *et al.*: A system for the high-throughput measurement of the shear modulus distribution of human red blood cells. Lab on a Chip **20**(16), 2927–2936 (2020)

ICCS Camera Ready Version 2025
To cite this paper please use the final published version:
DOI: 10.1007/978-3-031-97626-1_20

15. Don, M.: The Coulter principle: foundation of an industry. JALA: Journal of the Association for Laboratory Automation **8**(6), 72–81 (2003)
16. Kim, J., Han, S., Lei, A., Miyano, M., Bloom, J., Srivastava, V., *et al.*: Characterizing cellular mechanical phenotypes with mechano-node-pore sensing. Microsystems & nanoengineering **4**(1), 1–12 (2018)
17. Lai, A., Rex, R., Cotner, K.L., Dong, A., Lustig, M., Sohn, L.L.: Mechano-node-pore sensing: A rapid, label-free platform for multi-parameter single-cell viscoelastic measurements. JoVE (Journal of Visualized Experiments) (2022)
18. Saleh, O., Sohn, L.: Correcting off-axis effects in an on-chip resistive-pulse analyzer. Review of scientific instruments **73**(12), 4396–4398 (2002)
19. Randles, A.P., Kale, V., Hammond, J., Gropp, W., Kaxiras, E.: Performance analysis of the lattice Boltzmann model beyond Navier-Stokes. In: 2013 IEEE 27th International Symposium on Parallel and Distributed Processing, pp. 1063–1074 (2013)
20. Gounley, J., Draeger, E.W., Randles, A.: Numerical simulation of a compound capsule in a constricted microchannel. Procedia computer science **108**, 175–184 (2017)
21. Chen, S., Doolen, G.D.: Lattice Boltzmann method for fluid flows. Annual review of fluid mechanics **30**(1), 329–364 (1998)
22. Krüger, T., Kusumaatmaja, H., Kuzmin, A., Shardt, O., Silva, G., Viggen, E.M.: The lattice Boltzmann method. Springer International Publishing **10**(978-3), 4–15 (2017)
23. Guo, Z., Zheng, C., Shi, B.: Discrete lattice effects on the forcing term in the lattice Boltzmann method. Physical review E **65**(4), 046308 (2002)
24. Hecht, M., Harting, J.: Implementation of on-site velocity boundary conditions for D3Q19 lattice Boltzmann simulations. Journal of Statistical Mechanics: Theory and Experiment **2010**(01), P01018 (2010)
25. Krüger, T., Varnik, F., Raabe, D.: Efficient and accurate simulations of deformable particles immersed in a fluid using a combined immersed boundary lattice Boltzmann finite element method. Computers & Mathematics with Applications **61**(12), 3485–3505 (2011)
26. Skalak, R., Tozeren, A., Zarda, R., Chien, S.: Strain energy function of red blood cell membranes. Biophysical journal **13**(3), 245–264 (1973)
27. Zhong-Can, O.-Y., Helfrich, W.: Bending energy of vesicle membranes: General expressions for the first, second, and third variation of the shape energy and applications to spheres and cylinders. Physical Review A **39**(10), 5280 (1989)
28. Peskin, C.S.: The immersed boundary method. Acta numerica **11**, 479–517 (2002)
29. Zou, Q., He, X.: On pressure and velocity boundary conditions for the lattice Boltzmann BGK model. Physics of fluids **9**(6), 1591–1598 (1997)
30. Mietke, A., Otto, O., Girardo, S., Rosendahl, P., Taubenberger, A., Golfier, S., *et al.*: Extracting cell stiffness from real-time deformability cytometry: theory and experiment. Biophysical journal **109**(10), 2023–2036 (2015)
31. Ahmmed, S.M., Suteria, N.S., Garbin, V., Vanapalli, S.A.: Hydrodynamic mobility of confined polymeric particles, vesicles, and cancer cells in a square microchannel. Biomicrofluidics **12**(1) (2018)
32. Kuriakose, S., Dimitrakopoulos, P.: Motion of an elastic capsule in a square microfluidic channel. Physical Review E—Statistical, Nonlinear, and Soft Matter Physics **84**(1), 011906 (2011)

ICCS Camera Ready Version 2025
To cite this paper please use the final published version:
DOI: 10.1007/978-3-031-97626-1_20